

DRMC: A Generalist Model with Dynamic Routing for Multi-Center PET Image Synthesis

Zhiwen Yang¹, Yang Zhou¹, Hui Zhang², Bingzheng Wei³, Yubo Fan¹, and Yan Xu¹(✉,*)

¹ School of Biological Science and Medical Engineering, State Key Laboratory of Software Development Environment, Key Laboratory of Biomechanics and Mechanobiology of Ministry of Education, Beijing Advanced Innovation Center for Biomedical Engineering, Beihang University, Beijing 100191, China
xuyan04@gmail.com

² Department of Biomedical Engineering, Tsinghua University, Beijing 100084, China

³ Xiaomi Corporation, Beijing 100085, China

Abstract. Multi-center positron emission tomography (PET) image synthesis aims at recovering low-dose PET images from multiple different centers. The generalizability of existing methods can still be suboptimal for a multi-center study due to domain shifts, which result from non-identical data distribution among centers with different imaging systems/protocols. While some approaches address domain shifts by training specialized models for each center, they are parameter inefficient and do not well exploit the shared knowledge across centers. To address this, we develop a generalist model that shares architecture and parameters across centers to utilize the shared knowledge. However, the generalist model can suffer from the center interference issue, *i.e.* the gradient directions of different centers can be inconsistent or even opposite owing to the non-identical data distribution. To mitigate such interference, we introduce a novel dynamic routing strategy with cross-layer connections that routes data from different centers to different experts. Experiments show that our generalist model with dynamic routing (DRMC) exhibits excellent generalizability across centers. Code and data are available at: <https://github.com/Yaziwel/Multi-Center-PET-Image-Synthesis>.

Keywords: Multi-Center · Positron Emission Tomography · Synthesis · Generalist Model · Dynamic Routing.

1 Introduction

Positron emission tomography (PET) image synthesis [1,2,3,4,5,6,7,8,9,10] aims at recovering high-quality full-dose PET images from low-dose ones. Despite great success, most algorithms [1,2,4,5,8,9,10] are specialized for PET data from a single center with a fixed imaging system/protocol. This poses a significant problem for practical applications, which are not usually restricted to any one

* Corresponding author

of the centers. Towards filling this gap, in this paper, we focus on multi-center PET image synthesis, aiming at processing data from multiple different centers.

However, the generalizability of existing models can still be suboptimal for a multi-center study due to domain shift, which results from non-identical data distribution among centers with different imaging systems/protocols (see Fig. 1 (a)). Though some studies have shown that a specialized model (*i.e.* a convolutional neural network (CNN) [3,6] or Transformer [9] trained on a single center) exhibits certain robustness to different tracer types [9], different tracer doses [3], or even different centers [6], such generalizability of a center-specific knowledge is only applicable to small domain shifts. It will suffer a severe performance drop when exposed to new centers with large domain shifts [11]. There are also some federated learning (FL) based [12,11,7] medical image synthesis methods that improve generalizability by collaboratively learning a shared global model across centers. Especially, federated transfer learning (FTL) [7] first successfully applies FL to PET image synthesis in a multiple-dose setting. Since the resultant shared model of the basic FL method [12] ignores center specificity and thus cannot handle centers with large domain shifts, FTL addresses this by finetuning the shared model for each center/dose. However, FTL only focuses on different doses and does not really address the multi-center problem. Furthermore, it still requires a specialized model for each center/dose, which ignores potentially transferable shared knowledge across centers and scales up the overall model size.

A recent trend, known as generalist models, is to request that a single unified model works for multiple tasks/domains, and even express generalizability to novel tasks/domains. By sharing architecture and parameters, generalist models can better utilize shared transferable knowledge across tasks/domains. Some pioneers [13,14,15,16,17] have realized competitive performance on various high-level vision tasks like classification [13,16], object detection [14], *etc.*

Nonetheless, recent studies [18,16] report that conventional generalist [15] models may suffer from the interference issue, *i.e.* different tasks with shared parameters potentially conflict with each other in the update directions of the gradient. Specific to PET image synthesis, due to the non-identical data distribution across centers, we also observe the **center interference issue** that the gradient directions of different centers may be inconsistent or even opposite (see Fig. 1). This will lead to an uncertain update direction that deviates from the optimal, resulting in sub-optimal performance of the model. To address the interference issue, recent generalist models [14,16] have introduced dynamic routing [19] which learns to activate experts (*i.e.* sub-networks) dynamically. The input feature will be routed to different selected experts accordingly so as to avoid interference. Meanwhile, different inputs can share some experts, thus maintaining collaboration across domains. In the inference time, the model can reasonably generalize to different domains, even unknown domains, by utilizing the knowledge of existing experts. In spite of great success, the study of generalist models rarely targets the problem of multi-center PET image synthesis.

In this paper, inspired by the aforementioned studies, we innovatively propose a generalist model with **Dynamic Routing for Multi-Center** PET image

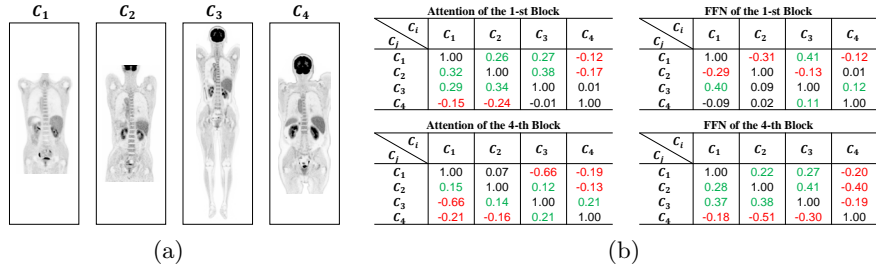


Fig. 1. (a) Examples of PET images at different Centers. There are domain shifts between centers. (b) The interference metric $\mathcal{I}_{i,j}$ [16] of the center C_j on the center C_i at the 1-st/4-th blocks as examples. The red value indicates that C_j has a negative impact on C_i , and the green value indicates that C_j has a positive impact on C_i .

synthesis, termed DRMC. To mitigate the center interference issue, we propose a novel dynamic routing strategy to route data from different centers to different experts. Compared with existing routing strategies, our strategy makes an improvement by building cross-layer connections for more accurate expert decisions. Extensive experiments show that DRMC achieves the best generalizability on both known and unknown centers. Our contribution can be summarized as:

- A generalist model called DRMC is proposed, which enables multi-center PET image synthesis with a single unified model.
- A novel dynamic routing strategy with cross-layer connection is proposed to address the center interference issue. It is realized by dynamically routing data from different centers to different experts.
- Extensive experiments show that DRMC exhibits excellent generalizability over multiple different centers.

2 Method

2.1 Center Interference Issue

Due to the non-identical data distribution across centers, different centers with shared parameters may conflict with each other in the optimization process. To verify this hypothesis, we train a baseline Transformer with 15 base blocks (Fig. 2 (b)) over four centers. Following the paper [16], we calculate the gradient direction interference metric $\mathcal{I}_{i,j}$ of the j -th center C_j on the i -th center C_i . As shown in Fig. 1 (b), interference is observed between different centers at different layers. This will lead to inconsistent optimization and inevitably degrade the model performance. Details of $\mathcal{I}_{i,j}$ [16] are shown in the **supplement**.

2.2 Network Architecture

The overall architecture of our DRMC is shown in Fig. 2 (a). DRMC firstly applies a $3 \times 3 \times 3$ convolutional layer for shallow feature extraction. Next, the

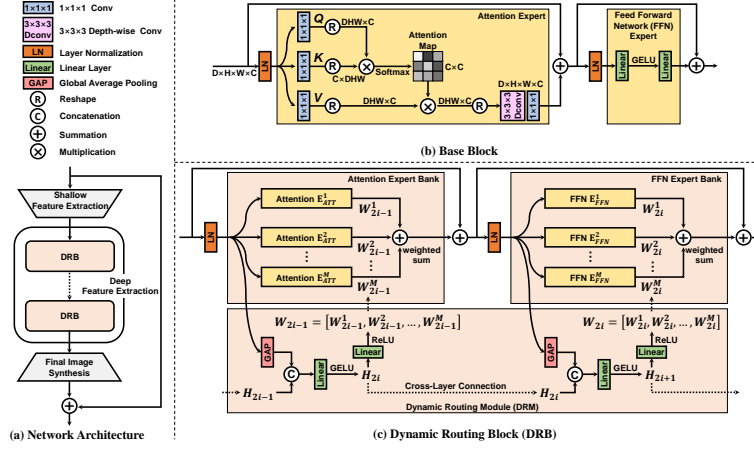


Fig. 2. The framework of our proposed DRMC

shallow feature is fed into N blocks with dynamic routing (DRBs), which are expected to handle the interference between centers and adaptively extract the deep feature with high-frequency information. The deep feature then passes through another $3 \times 3 \times 3$ convolutional layer for final image synthesis. In order to alleviate the burden of feature learning and stabilize training, DRMC adopts global residual learning as suggested in the paper [20] to estimate the image residual from different centers. In the subsequent subsection, we will expatiate the dynamic routing strategy as well as the design of the DRB.

2.3 Dynamic Routing Strategy

We aim at alleviating the center interference issue in deep feature extraction. Inspired by prior generalist models [13,14,16], we specifically propose a novel dynamic routing strategy for multi-center PET image synthesis. The proposed dynamic routing strategy can be flexibly adapted to various network architectures, such as CNN and Transformer. To utilize the recent advance in capturing global contexts using Transformers [9], without loss of generality, we explore the application of the dynamic routing strategy to a Transformer block, termed dynamic routing block (DRB, see Fig. 2 (c)). We will introduce our dynamic routing strategy in detail from four parts: base expert foundation, expert number scaling, expert dynamic routing, and expert sparse fusion.

Base Expert Foundation. As shown in Figure 2 (b), we first introduce an efficient base Transformer block (base block) consisting of an attention expert and a feed-forward network (FFN) expert. Both experts are for basic feature extraction and transformation. To reduce the complexity burden of the attention expert, we follow the paper [9] to perform global channel attention with linear complexity instead of spatial attention [21]. Notably, as the global channel attention may ignore the local spatial information, we introduce depth-wise convolutions

to emphasize the local context after applying attention. As for the FFN expert, we make no modifications to it compared with the standard Transformer block [21]. It consists of a 2-layer MLP with GELU activation in between.

Expert Number Scaling. Center interference is observed on both attention experts and FFN experts at different layers (see Fig. 1 (b)). This indicates that a single expert can not be simply shared by all centers. Thus, we increase the number of experts in the base block to M to serve as expert candidates for different centers. Specifically, each Transformer block has an attention expert bank $\mathbf{E}_{ATT} = [\mathbf{E}_{ATT}^1, \mathbf{E}_{ATT}^2, \dots, \mathbf{E}_{ATT}^M]$ and an FFN expert bank $\mathbf{E}_{FFN} = [\mathbf{E}_{FFN}^1, \mathbf{E}_{FFN}^2, \dots, \mathbf{E}_{FFN}^M]$, both of which have M base experts. However, it does not mean that we prepare specific experts for each center. Although using center-specific experts can address the interference problem, it is hard for the model to exploit the shared knowledge across centers, and it is also difficult to generalize to new centers that did not emerge in the training stage [16]. To address this, we turn to different combinations of experts.

Expert Dynamic Routing. Given a bank of experts, we route data from different centers to different experts so as to avoid interference. Prior generalist models [13,14,16] in high-level vision tasks have introduced various routing strategies to weigh and select experts. Most of them are independently conditioned on the information of the current layer feature, failing to take into account the connectivity of neighboring layers. Nevertheless, PET image synthesis is a dense prediction task that requires a tight connection of adjacent layers for accurate voxel-wise intensity regression. To mitigate the potential discontinuity [13], we propose a dynamic routing module (DRM, see Fig. 2 (c)) that builds cross-layer connection for expert decisions. The mechanism can be formulated as:

$$W = \text{ReLU}(\text{MLP}([\text{GAP}(X), H])), \quad (1)$$

where X denotes the input; $\text{GAP}(\cdot)$ represents the global average pooling operation to aggregate global context information of the current layer; H is the hidden representation of the previous MLP layer. ReLU activation generates sparsity by setting the negative weight to zero. It is a more suitable gating function in comparison with the commonly used softmax activation [14] and top-k gating [13,16] in our study (see Table. 4). W is a sparse weight used to assign weights to different experts.

In short, DRM sparsely activates the model and selectively routes the input to different subsets of experts. This process maximizes collaboration and meanwhile mitigates the interference problem. On the one hand, the interference across centers can be alleviated by sparsely routing X to different experts (with positive weights). The combinations of selected experts can be thoroughly different across centers if violent conflicts appear. On the other hand, experts in the same bank still cooperate with each other, allowing the network to best utilize the shared knowledge across centers.

Expert Sparse Fusion. The final output is a weighted sum of each expert’s knowledge using the sparse weight $W = [W^1, W^2, \dots, W^M]$ generated by DRM.

Table 1. Multi-Center PET Dataset Information

Center	Institution	Type	Lesion	System	Tracer	Dose	DRF	Spacing (mm^3)	Shape	Train	Test	
C_{kn}	C_1	I_1	Whole Body	Yes	PolarStar m660	^{18}F -FDG	293MBq	12	$3.15 \times 3.15 \times 1.87$	$192 \times 192 \times slices$	20	10
	C_2	I_2	Whole Body	Yes	PolarStar Flight	^{18}F -FDG	293MBq	4	$3.12 \times 3.12 \times 1.75$	$192 \times 192 \times slices$	20	10
	C_3 [22]	I_3	Whole Body	Yes	United Imaging uEXPLORER	^{18}F -FDG	296MBq	10	$1.67 \times 1.67 \times 2.89$	$256 \times 256 \times slices$	20	10
	C_4 [22]	I_4	Whole Body	Yes	Siemens Biograph Vision Quadra	^{18}F -FDG	296MBq	10	$1.65 \times 1.65 \times 1.65$	$256 \times 256 \times slices$	20	10
C_{ukn}	C_5	I_5	Brain	No	PolarStar m660	^{18}F -FDG	293MBq	4	$1.18 \times 1.18 \times 1.87$	$256 \times 256 \times slices$	-	10
	C_6	I_6	Whole Body	Yes	PolarStar m660	^{18}F -FDG	293MBq	12	$3.15 \times 3.15 \times 1.87$	$192 \times 192 \times slices$	-	10

Given an input feature X , the output \hat{X} of an expert bank can be obtained as:

$$\hat{X} = \sum_{m=1}^M W^m \cdot \mathbf{E}^m(X), \quad (2)$$

where $\mathbf{E}^m(\cdot)$ represents an operator of $\mathbf{E}_{ATT}^m(\cdot)$ or $\mathbf{E}_{FFN}^m(\cdot)$.

2.4 Loss Function

We utilize the Charbonnier loss [23] with hyper-parameter ϵ as 10^{-3} to penalize pixel-wise differences between the full-dose (Y) and estimated (\hat{Y}) PET images:

$$\mathcal{L} = \sqrt{\|Y - \hat{Y}\|^2 + \epsilon^2}. \quad (3)$$

3 Experiments and Results

3.1 Dataset and Evaluation

Full-dose PET images are collected from 6 different centers (C_1 – C_6) at 6 different institutions¹. The data of C_3 and C_4 [22] are borrowed from the Ultra-low Dose PET Imaging Challenge², while the data from other centers were privately collected. The key information of the whole dataset is shown in Table. 1. Note that C_1 – C_4 are for both training and testing. We denote them as C_{kn} as these centers are known to the generalist model. C_5 and C_6 are unknown centers (denote as C_{ukn}) that are only for testing the model generalizability. The low-dose PET data is generated by randomly selecting a certain portion of the raw scans according to the dose reduction factor (DRF), *e.g.* the portion is 25% when DRF=4. Then we reconstruct low-dose PET images using the standard OSEM method [24]. Since the voxel size differs across centers, we uniformly resample

¹ I_1 and I_5 are Peking Union Medical College Hospital; I_2 is Beijing Hospital; I_3 is Department of Nuclear Medicine, Ruijin Hospital, Shanghai Jiao Tong University School of Medicine; I_4 is Department of Nuclear Medicine, University of Bern; I_6 is Beijing Friendship Hospital.

² Challenge site: <https://ultra-low-dose-pet.grand-challenge.org/>. The investigators of the challenge contributed to the design and implementation of DATA, but did not participate in analysis or writing of this paper. A complete listing of investigators can be found at: <https://ultra-low-dose-pet.grand-challenge.org/Description/>.

Table 2. Results on C_{kn} . The **Best** and the **Second-Best** Results are Highlighted.
*: Significant Difference at $p < 0.05$ between Comparison Method and Our Method.

Methods	PSNR \uparrow					$B_{mean}\downarrow$					$B_{max}\downarrow$				
	C_1	C_2	C_3	C_4	Avg.	C_1	C_2	C_3	C_4	Avg.	C_1	C_2	C_3	C_4	Avg.
(i) 3D-cGAN	47.30*	44.97*	45.15*	43.08*	45.13*	0.0968*	0.0832	0.0795*	0.1681*	0.1069*	0.1358*	0.1696*	0.1726*	0.2804*	0.1896*
3D CVT-GAN	47.46*	45.17*	45.94*	44.04*	45.65*	0.0879	0.0972*	0.0594*	0.1413*	0.0965*	0.1178*	0.1591*	0.1652*	0.2224*	0.1661*
FedAVG	47.43*	44.62*	45.61*	43.75*	45.35*	0.0985*	0.0996*	0.1006*	0.2202*	0.1122*	0.1459*	0.1546*	0.2011*	0.2663*	0.1920*
(ii) FL-MRCM	47.81*	45.56*	46.10*	44.31*	45.95*	0.0939*	0.0929*	0.0631*	0.1344*	0.0961*	0.1571*	0.1607*	0.1307*	0.1518*	0.1501*
FTL	48.05*	45.62*	46.01*	44.75*	46.11*	0.0892	0.0945*	0.0587*	0.0895	0.0830*	0.1243*	0.1588*	0.0893	0.1436	0.1290*
DRMC	49.48	46.32	46.71	45.01	46.88	0.0844	0.0792	0.0491	0.0880	0.0752	0.1037	0.1313	0.0837	0.1431	0.1155

Table 3. Results on C_{ukn} .

Methods	PSNR \uparrow		$B_{mean}\downarrow$		$B_{max}\downarrow$	
	C_5	C_6	C_5	C_6	C_5	C_6
(i) 3D-cGAN	26.53*	46.07*	-	0.1956*	-	0.1642*
3D CVT-GAN	27.11*	46.03*	-	0.1828	-	0.1686*
FedAVG	27.09*	46.48*	-	0.1943*	-	0.2291*
(ii) FL-MRCM	25.38*	47.08*	-	0.1998*	-	0.1762*
FTL	27.38*	48.05*	-	0.1898*	-	0.1556*
DRMC	28.54	48.26	-	0.1814	-	0.1483

Table 4. Routing Ablation Results.

Methods	C_{kn}			C_{ukn}		
	PSNR \uparrow	$B_{mean}\downarrow$	$B_{max}\downarrow$	PSNR \uparrow	$B_{mean}\downarrow$	$B_{max}\downarrow$
w/o H	46.64*	0.0907*	0.1436*	38.23*	0.1826	0.1548*
Softmax	46.70*	0.0849*	0.1277*	38.33	0.1864*	0.1524*
Top-2 Gating	46.61*	0.0896*	0.1295*	38.38	0.1867*	0.1564*
DRMC	46.88	0.0752	0.1155	38.40	0.1814	0.1483

the images of different centers so that their voxel size becomes $2 \times 2 \times 2 \text{ mm}^3$. In the training phase, we unfold images into small patches (uniformly sampling 1024 patches from 20 patients per center) with a shape of $64 \times 64 \times 64$. In the testing phase, the whole estimated PET image is acquired by merging patches together.

To evaluate the model performance, we choose the PSNR metric for image quantitative evaluation. For clinical evaluation, to address the accuracy of the standard uptake value (SUV) that most radiologists care about, we follow the paper [3] to calculate the bias of SUV_{mean} and SUV_{max} (denoted as B_{mean} and B_{max} , respectively) between low-dose and full-dose images in lesion regions.

3.2 Implementation

Unless specified otherwise, the intermediate channel number, expert number in a bank, and Transformer block number are 64, 3, and 5, respectively. We employ Adam optimizer with a learning rate of 10^{-4} . We implement our method with Pytorch using a workstation with 4 NVIDIA A100 GPUs with 40GB memory (1 GPU per center). In each training iteration, each GPU independently samples data from a single center. After the loss calculation and the gradient back-propagation, the gradients of different GPUs are then synchronized. We train our model for 200 epochs in total as no significant improvement afterward.

3.3 Comparative Experiments

We compare our method with five methods of two types. (i) 3D-cGAN [1] and 3D CVT-GAN [10] are two state-of-the-art methods for single center PET image synthesis. (ii) FedAVG[12,11], FL-MRCM[11], and FTL[7] are three federated learning methods for privacy-preserving multi-center medical image synthesis.

Table 5. Comparison results for Specialized Models and Generalist Models.

Methods	Train Centers	PSNR \uparrow					$B_{mean}\downarrow$					$B_{max}\downarrow$					
		Test Centers				Avg.	Test Centers				Avg.	Test Centers				Avg.	
		C_1	C_2	C_3	C_4		C_1	C_2	C_3	C_4		C_1	C_2	C_3	C_4		
Specialized Model	Baseline	C_1	48.89*	45.06*	43.94*	41.55*	44.86*	0.0849	0.0949*	0.1490*	0.2805*	0.1523*	0.1207*	0.1498*	0.3574*	0.4713*	0.2748*
		C_2	47.05*	46.08*	43.82*	41.53*	44.62*	0.0933*	0.0557*	0.1915*	0.2247*	0.1413*	0.1326*	0.1243*	0.3275*	0.4399*	0.2561*
		C_3	44.04*	41.00*	46.52*	44.07*	44.11*	0.2366*	0.2111*	0.0446	0.1364*	0.1572*	0.4351*	0.5567*	0.0729*	0.1868*	0.3129*
		C_4	44.41*	41.39*	46.01*	44.95	44.29*	0.2462*	0.2063*	0.0897*	0.0966*	0.1597*	0.4887*	0.5882*	0.1222*	0.1562*	0.3388*
Generalist Model	Baseline	C_1, C_2, C_3, C_4	47.59*	44.73*	46.02*	44.20*	45.64*	0.0924*	0.0839*	0.0844*	0.1798*	0.1101*	0.1424*	0.1424*	0.1579*	0.2531*	0.1740*
	DRMC	C_1, C_2, C_3, C_4	49.48	46.32	46.71	45.01	46.88	0.0844	0.0792	0.0491	0.0880	0.0752	0.1037	0.1313	0.0837	0.1431	0.1155

All methods are trained using data from C_{kn} and tested over both C_{kn} and C_{ukn} . For methods in (i), we regard C_{kn} as a single center and mix all data together for training. For federated learning methods in (ii), we follow the "Mix" mode (upper bound of FL-based methods) in the paper [11] to remove the privacy constraint and keep the problem setting consistent with our multi-center study.

Comparison Results for Known Centers. As can be seen in Table. 2, in comparison with the second-best results, DRMC boosts the performance by 0.77 dB PSNR, 0.0078 B_{mean} , and 0.0135 B_{max} . This is because our DRMC not only leverages shared knowledge by sharing some experts but also preserves center-specific information with the help of the sparse routing strategy. Further evaluation can be found in the **supplement**.

Comparison Results for Unknown Centers. We also test the model generalization ability to unknown centers C_5 and C_6 . C_5 consists of normal brain data (without lesion) that is challenging for generalization. As the brain region only occupies a small portion of the whole-body data in the training dataset but has more sophisticated structure information. C_6 is a similar center to C_1 but has different working locations and imaging preferences. The quantitative results are shown in Table. 3 and the visual results are shown in Fig. 1 (a). DRMC achieves the best results by dynamically utilizing existing experts' knowledge for generalization. On the contrary, most comparison methods process data in a static pattern and unavoidably produce mishandling of out-of-distribution data.

Furthermore, we evaluate the performance of different models on various DRF data on C_6 , and the results are available in the **supplement**. These results indicate that our method demonstrates strong robustness.

3.4 Ablation Study

Specialized Model vs. Generalist Model. As can be seen in Table. 5, the baseline model (using 15 base blocks) individually trained for each center acquires good performance on its source center. But it suffers performance drop on other centers. The baseline model trained over multiple centers greatly enhances the overall results. But due to the center interference issue, its performance on a specific center is still far from the corresponding specialized model. DRMC mitigates the interference with dynamic routing and achieves comparable performance to the specialized model of each center.

Ablation Study of Routing Strategy. To investigate the roles of major components in our routing strategy, we conduct ablation studies through (i) removing

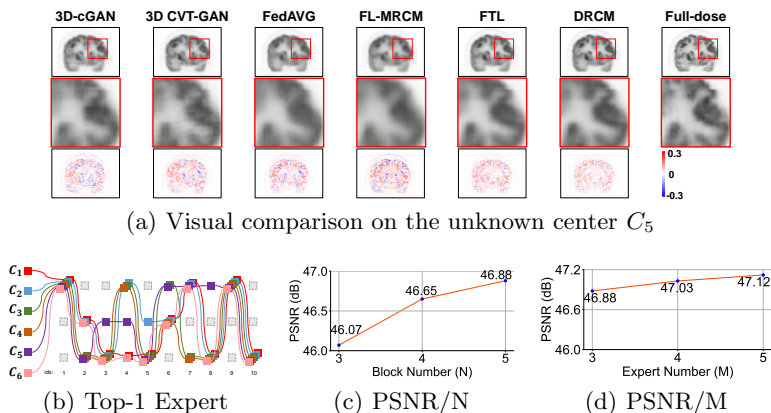


Fig. 3. Figures of different experiments.

the condition of hidden representation H that builds cross-layer connection, and replacing ReLU activation with (ii) softmax activation [14] and (iii) top-2 gating [13]. The results are shown in Table. 4. We also analyze the interpretability of the routing by showing the distribution of different layers' top-1 weighted experts using the testing data. As shown in Fig. 3 (b), different centers show similarities and differences in the expert distribution. For example, C_6 shows the same distribution with C_1 as their data show many similarities, while C_5 presents a very unique way since brain data differs a lot from whole-body data.

Ablation Study of Hyperparameters. In Fig. 3 (c) and (d), we show ablation results on expert number (M) and block number (N). We set $M=3$ and $N=5$, as this configuration has demonstrated good performance while maintaining acceptable computational complexity.

4 Conclusion

In this paper, we innovatively propose a generalist model with dynamic routing (DRMC) for multi-center PET image synthesis. To address the center interference issue, DRMC sparsely routes data from different centers to different experts. Experiments show that DRMC achieves excellent generalizability.

References

1. Wang, Y., Yu, B., Wang, L., Zu, C., Lin, W., Wu, X., Zhou, J., Zhou, L.: 3d conditional generative adversarial networks for high-quality pet image estimation at low dose. *NeuroImage* **174** (03 2018)
2. Xiang, L., Qiao, Y., Nie, D., An, L., Lin, W., Wang, Q., Shen, D.: Deep auto-context convolutional neural networks for standard-dose pet image estimation from low-dose pet/mri. *Neurocomputing* **267**, 406–416 (2017)

3. Zhou, L., Schaefferkoetter, J., Tham, I., Huang, G., Yan, J.: Supervised learning with cyclegan for low-dose fdg pet image denoising. *Medical Image Analysis* **65**, 101770 (07 2020)
4. Zhou, Y., Yang, Z., Zhang, H., Chang, E.I.C., Fan, Y., Xu, Y.: 3d segmentation guided style-based generative adversarial networks for pet synthesis. *IEEE Transactions on Medical Imaging* **41**(8), 2092–2104 (2022)
5. Luo, Y., Zhou, L., Zhan, B., Fei, Y., Zhou, J., Wang, Y.: Adaptive rectification based adversarial network with spectrum constraint for high-quality pet image synthesis. *Medical Image Analysis* **77**, 102335 (12 2021)
6. Chaudhari, A., Mitra, E., Davidzon, G., Gulaka, P., Gandhi, H., Brown, A., Zhang, T., Srinivas, S., Gong, E., Zaharchuk, G., Jadvar, H.: Low-count whole-body pet with deep learning in a multicenter and externally validated study. *npj Digital Medicine* **4**, 127 (08 2021)
7. Zhou, B., Miao, T., Mirian, N., Chen, X., Xie, H., Feng, Z., Guo, X., Li, X., Zhou, S.K., Duncan, J.S., Liu, C.: Federated transfer learning for low-dose pet denoising: A pilot study with simulated heterogeneous data. *IEEE Transactions on Radiation and Plasma Medical Sciences* pp. 1–1 (2022)
8. Luo, Y., Wang, Y., Zu, C., Zhan, B., Wu, X., Zhou, J., Shen, D., Zhou, L.: 3d transformer-gan for high-quality pet reconstruction. In: de Bruijne, M., Cattin, P.C., Cotin, S., Padoy, N., Speidel, S., Zheng, Y., Essert, C. (eds.) *Medical Image Computing and Computer Assisted Intervention – MICCAI 2021*. pp. 276–285. Springer International Publishing, Cham (2021)
9. Jang, S.I., Pan, T., Li, Y., Heidari, P., Chen, J., Li, Q., Gong, K.: Spach transformer: Spatial and channel-wise transformer based on local and global self-attentions for pet image denoising (09 2022)
10. Zeng, P., Zhou, L., Zu, C., Zeng, X., Jiao, Z., Wu, X., Zhou, J., Wang, Y.: 3D CVT-GAN: A 3D Convolutional Vision Transformer-GAN for PET Reconstruction, pp. 516–526 (09 2022)
11. Guo, P., Wang, P., Zhou, J., Jiang, S., Patel, V.M.: Multi-institutional collaborations for improving deep learning-based magnetic resonance image reconstruction using federated learning. In: *Proceedings of the IEEE/CVF Conference on Computer Vision and Pattern Recognition (CVPR)*. pp. 2423–2432 (June 2021)
12. McMahan, H.B., Moore, E., Ramage, D., Hampson, S., et al.: Communication-efficient learning of deep networks from decentralized data. *arXiv preprint arXiv:1602.05629* (2016)
13. Shazeer, N., Mirhoseini, A., Maziarz, K., Davis, A., Le, Q., Hinton, G., Dean, J.: Outrageously large neural networks: The sparsely-gated mixture-of-experts layer (01 2017)
14. Wang, X., Cai, Z., Gao, D., Vasconcelos, N.: Towards universal object detection by domain attention. In: *Proceedings of the IEEE Conference on Computer Vision and Pattern Recognition*. pp. 7289–7298 (2019)
15. Zhu, X., Zhu, J., Li, H., Wu, X., Wang, X., Li, H., Wang, X., Dai, J.: Uni-perceiver: Pre-training unified architecture for generic perception for zero-shot and few-shot tasks. *arXiv preprint arXiv:2112.01522* (2021)
16. Zhu, J., Zhu, X., Wang, W., Wang, X., Li, H., Wang, X., Dai, J.: Uni-perceiver-moe: Learning sparse generalist models with conditional moes. In: Oh, A.H., Agarwal, A., Belgrave, D., Cho, K. (eds.) *Advances in Neural Information Processing Systems* (2022)
17. Wang, P., Yang, A., Men, R., Lin, J., Bai, S., Li, Z., Ma, J., Zhou, C., Zhou, J., Yang, H.: Ofa: Unifying architectures, tasks, and modalities through a simple sequence-to-sequence learning framework. *CoRR* **abs/2202.03052** (2022)

18. Yu, T., Kumar, S., Gupta, A., Levine, S., Hausman, K., Finn, C.: Gradient surgery for multi-task learning. arXiv preprint arXiv:2001.06782 (2020)
19. Han, Y., Huang, G., Song, S., Yang, L., Wang, H., Wang, Y.: Dynamic neural networks: A survey (02 2021)
20. Zhang, K., Zuo, W., Chen, Y., Meng, D., Zhang, L.: Beyond a gaussian denoiser: Residual learning of deep cnn for image denoising. *IEEE Transactions on Image Processing* **26**(7), 3142–3155 (2017)
21. Vaswani, A., Shazeer, N., Parmar, N., Uszkoreit, J., Jones, L., Gomez, A.N., Kaiser, L., Polosukhin, I.: Attention is all you need. In: *Advances in Neural Information Processing Systems*. pp. 5998–6008 (2017)
22. Xue, S., Guo, R., Bohn, K.P., Matzke, J., Viscione, M., Alberts, I., Meng, H., Sun, C., Zhang, M., Zhang, M., Sznitman, R., El Fakhri, G., Rominger, A., Li, B., Shi, K.: A cross-scanner and cross-tracer deep learning method for the recovery of standard-dose imaging quality from low-dose pet. *European Journal of Nuclear Medicine and Molecular Imaging* **49**, 1619–7089 (05 2022)
23. Charbonnier, P., Blanc-Feraud, L., Aubert, G., Barlaud, M.: Two deterministic half-quadratic regularization algorithms for computed imaging. In: *Proceedings of 1st International Conference on Image Processing*. vol. 2, pp. 168–172 vol.2 (1994)
24. Hudson, H., Larkin, R.: Accelerated image reconstruction using ordered subsets of projection data. *IEEE Transactions on Medical Imaging* **13**(4), 601–609 (1994)

Supplement

Center Interference. To quantify the interference of the j -th center task on the i -th center task, we estimate the change in loss \mathcal{L}_i for the i -th center task when optimizing the shared parameters θ according to the j -th center task’s loss \mathcal{L}_j as follows:

$$\begin{aligned} \Delta_j \mathcal{L}_i(X_i) &\doteq \mathbb{E}_{X_j} \left(\mathcal{L}_i(X_i; \theta) - \mathcal{L}_i(X_i; \theta - \lambda \frac{\nabla_{\theta} \mathcal{L}_j(X_j)}{\|\nabla_{\theta} \mathcal{L}_j(X_j)\|}) \right), \\ &\approx \lambda \mathbb{E}_{X_j} \left(\frac{\nabla_{\theta} \mathcal{L}_j(X_j)}{\|\nabla_{\theta} \mathcal{L}_j(X_j)\|}^T \nabla_{\theta} \mathcal{L}_i(X_i) \right), \end{aligned} \quad (4)$$

where X_i and X_j are the sampled training batches of the i -th and j -th centers, respectively. In the implementation, we sample 100 batches from each center for interference calculation. The interference of the j -th center task on the i -th center task can then be quantified as follows:

$$\mathcal{I}_{i,j} = \mathbb{E}_{X_i} \left(\frac{\Delta_j \mathcal{L}_i(X_i)}{\Delta_i \mathcal{L}_i(X_i)} \right), \quad (5)$$

where the denominator is utilized to normalize the scale of the loss change.

SSIM Evaluation. To further assess the performance of our method, we compare the SSIM metric between our method and other comparison methods. The results are presented in Table 6. The results indicate that DRMC achieves the highest performance on the SSIM metric.

Table 6. SSIM Results on C_{kn} . The **Best** and the Second-Best Results are Highlighted. *: Significant Difference at $p < 0.05$ between Comparison Method and Our Method.

Methods	SSIM				
	C_1	C_2	C_3	C_4	Avg.
(i) 3D-cGAN	0.8524*	0.8267*	0.8077*	0.7972*	0.8210*
3D CVT-GAN	0.8837*	0.8931*	<u>0.9198*</u>	0.8770*	0.8934*
FedAVG	0.8997*	<u>0.9091*</u>	0.9188*	0.8802*	<u>0.9020*</u>
(ii) FL-MRCM	0.8960*	0.8812*	0.8777*	0.8482*	0.8758*
FTL	<u>0.9045*</u>	0.8889*	0.9056*	<u>0.8816*</u>	0.8952*
DRMC	0.9173	0.9172	0.9284	0.9010	0.9160

Evaluation on Different DRF Data. To verify the robustness of the model on different dosage data, we conducted tests on the unknown center C_6 . Table 7 presents the comparison results, demonstrating that our DRMC exhibits superior generalizability across different DRF data.

Table 7. Testing Results on Different DRF Data from C_6 . The **Best** and the **Second-Best** Results are Highlighted. *: Significant Difference at $p < 0.05$ between Comparison Method and Our Method.

Methods	PSNR				B_{mean}				B_{max}						
	DRF=3	DRF=4	DRF=6	DRF=12	Avg.	DRF=3	DRF=4	DRF=6	DRF=12	Avg.	DRF=3	DRF=4	DRF=6	DRF=12	Avg.
(i) 3D-cGAN	48.79*	48.63*	47.86*	46.07*	47.84*	0.0881*	0.0886*	0.1024*	0.1956*	0.1187	0.0653*	0.0744*	0.1086*	0.1642*	0.1031*
3D CVT-GAN	48.85*	48.57*	47.87*	46.03*	47.83*	0.0951*	0.1028*	0.1191*	0.1828*	0.1250	0.0677*	0.0821*	0.1032*	0.1686*	0.1054*
FedAVG	48.17*	48.23*	47.89*	46.48*	47.69*	0.1112*	0.1258*	0.1303*	0.1943*	0.1404	0.0624*	0.0781*	0.1021*	0.2291*	0.1179*
(ii) FL-MRCM	50.49*	50.21*	48.65*	47.08*	49.11*	0.1012*	0.1038*	0.1042*	0.1998*	0.1273	0.0543*	0.0956*	0.1041*	0.1762*	0.1076*
FTL	51.01	50.89	49.43*	48.05*	49.85*	0.0553*	0.0878	0.0986*	0.1898*	0.1079*	0.0484	0.0524*	0.0724*	0.1556*	0.0822*
(iii) DRMC	51.04	50.95	49.59	48.26	49.96	0.0438	0.0836	0.0929	0.1814	0.1004	0.0455	0.0457	0.0655	0.1483	0.0763